COBEM 2021 26th International Congress of Mechanical Engineering
November 22-26, 2021, Virtual Congress, Brazil
ABCM Associação Brasileira de Engenharia e Ciências Mecânicas

COB-2021-2210
Effects of hydrodynamic and thermo-diffusive instabilities in the local burning rate of lean premixed hydrogen/air laminar flames

Rafael Becker Meier
Amir Antônio Martins Oliveira
Universidade Federal de Santa Catarina
rafael.meier@labcet.ufsc.br
amir.oliveira@gmail.com

Abstract. *Flame surface instability is present in turbulent premixed flame propagation in the flamelet and corrugated flamelet regimes, strongly affecting the turbulent flame speed. In this work, direct numerical simulations are used to evaluate the linear and non-linear growth of instabilities caused by initial perturbations in lean hydrogen/air premixed flames. The numerical simulations employ multi-step chemistry and detailed transport in two-dimensional channels with periodic boundary conditions along the vertical boundaries. These flames present Lewis numbers smaller than the unit, and flame propagation is affected by both hydrodynamic and thermo-diffusive instabilities. A dispersion relation diagram mapping the perturbation growth rates and wavenumbers is compared to the literature data, validating the predictions. The stretch rate and thermo-diffusive instabilities in a Bunsen flame and a planar flame are compared. Then, the growth rates' effect on the local burning rate at the flame front are assessed and compared to steady-state stretch rates. The comparison reveals that, in regions where the stretch is weaker, the spectrum of curvature and wavelengths tends to keep the relation of flame speed and curvature as predicted by the linear theory despite the chaotic behavior of the wrinkled front. On the other hand, when the flame front curvature grows towards high negative values, the results increase the deviation from the linear model.*

Keywords: *Direct numerical simulations, hydrodynamic and thermo-diffusive instabilities, lean hydrogen/air premixed flames.*

1. INTRODUCTION

Fit the current power generation and transportation devices to renewable sources is one of the upcoming challenges in combustion technology. Even with petroleum dominance as the energy carrier in the last century, hydrogen has never been put aside in the scientific community since it generates energy without carbon dioxide emissions. The recent interest rising comes up with the concept of electrofuels (e-fuels) which all production chain starts from water and renewable electricity producing, primarily, H_2, Masri (2021). However, the e-fuels application to internal combustion engines and meanly to gas turbines presents some issues, Goldmann *et al.* (2018), Omari *et al.* (2019) and Lhuillier *et al.* (2020). In particular, lean hydrogen/air flames are prone to combustion instabilities, substantially changing flame dynamics and heat release rates. The interaction of such instabilities with turbulence cannot be accurately predicted with present-day combustion models. In most cases in turbulent flames, these instabilities are often neglected. However, recent researches suggest that thermo-diffusive mechanism could be the source of additional flame wrinkling in turbulent flames, Poinsot and Veynante (2005); Berger *et al.* (2019). In practical systems, flame instabilities can act as a double-edged sword. For instance, they can create conditions that may cause damage and mechanical failure to the combustion device. On the other hand, they may be favorable for enhancing mixing and increasing burn rates, Matalon (2007).

Flame instabilities are caused due to two different mechanism; the hydrodynamic instability and thermo-diffusive instability. The first one arises from the density jump across the flame, which gives the wrinkled aspect to the front. The streamline widening and narrowing decelerate the flow ahead of flame such that this effect is always destabilizing yielding an exponential amplitude growth, $A \sim \mathrm{e}^{(iky+\omega t)}$. This physical process is always present in any flame being an intrinsic combustion property. The thermo-diffusive effects can act in both directions, it can contribute to the destabilization increasing or may causes the formation of cellular structures die due to differential diffusion. The mechanism dynamics depends on the balance between heat and mass diffusion.

Experiments carried out in spherical bombs, shown in Fig. 1, are able to show the development of instabilities, Kwon *et al.* (2002) and Jomaas *et al.* (2007). For rich hydrocarbon-air or lean-hydrogen air mixtures, characterized by a Lewis number sufficiently less than one, the cellular appearance takes place shortly after the ignition. Contrarily, lean hydrocarbon-air and rich-hydrogen air mixtures, the formation of cellular structures only occurs if the hot radius is larger than a critical value. Before, the flame front curvature is large, and due to the high Lewis number, the molecular diffusion

exerts a stabilizing influence on the small disturbances damping the expansion effect. After the flame reaches the critical size, the thermal expansion dominates the process giving rise to the cellular appearance.

$\phi = 0.6, \mathrm{Le} < 1$ $\phi = 2.5, \mathrm{Le} > 1$

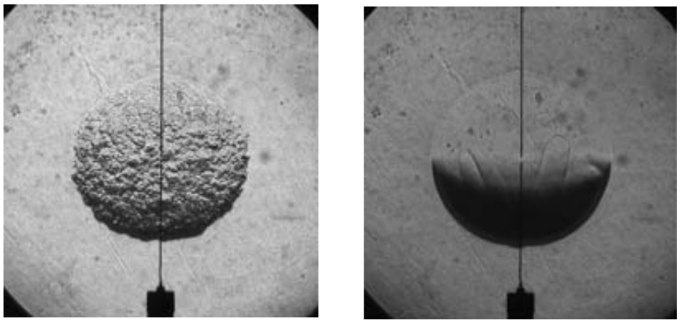

Figure 1: Schlieren images of outwardly propagating spherical flames of hydrogen-air for $\phi = 0.6$ and $\phi = 2.5$ at $p = 5$ atm. Source Jomaas *et al.* (2007).

This work intends to study the hydrodynamic and thermo-diffusive effects in two canonical flames, a Bunsen flame, and planar flames, using direct numerical simulations. The paper is divided into two parts. In the first one, the Bunsen flame is assessed regarding the stretch-chemistry interaction in which the thermo-diffusive instabilities can be isolated from the hydrodynamic influence. For the planar flames, the instabilities linear growth are evaluated, taking into account a range of perturbations wavelengths in order to map the dynamics of cellular structure formation. Further, a broad domain and full-time simulation will be performed with the aim to observe the spectrum of curvature wavelengths at the flame front and compute how the burning rate is affected by the surface deformation.

2. THEORETICAL BACKGROUND

2.1 Hydrodynamic theory

The local flame speed, Eq. (1), depends on the nominal flame speed and a constant variable $\mathscr{L}$, called Markstein length, and the local flame stretch rate K,

$$S_l = S_l^0 - \mathscr{L}\mathrm{K}. \tag{1}$$

In a Taylor expansion, the $\mathscr{L}$ represents, mathematically, the flame sensitivity to weak deformations. From a physical point of view, the Markstein length describes the influences of the diffusion process occurring within the flame zone. In more detailed modeling, Matalon *et al.* (2003) show the dependence on $\mathscr{L}$ with effects of stoichiometry, variable transport coefficients and arbitrary reaction orders. The flame stretch rate, Eq. (2), measures the front area deformation resulting from its motion and nonuniformities in the underlying flow field,

$$\mathrm{K} = \frac{1}{A}\frac{dA}{dt} = \mathrm{K_s} + \mathrm{K_c}. \tag{2}$$

The total stretch is a sum of strain rate, $\mathrm{K_s} = \nabla_t \cdot \vec{u}_o$, and the curvature rate, $\mathrm{K_c} = S_d\kappa$. Both terms are computed in the flame surface coordinates wherein an arbitrary isoline inside the front defines it. In the $\mathrm{K_c}$ term, S_d is the local displacement speed, and κ defines the front curvature, $\kappa = \nabla \cdot \vec{n}$. For a meaningful comparison between values of the displacement speed defined at different locations, S_d is often normalized by the ratio of local density ρ to the density of the fresh mixture ρ_u yielding, $\tilde{S}_d = \rho S_d/\rho_u$. The density-weighted flame displacement speed, $\tilde{S}_d$, can be directly compared to the laminar flame speed S_l^0 for the same reactant mixture. Using δ_l^0 and S_l^0 as characteristic length and velocity scales, the nondimensional form of Eq. (1) becomes,

$$\frac{S_l}{S_l^0} = 1 - \mathrm{Ma}\,\mathrm{Ka}, \tag{3}$$

where $\mathrm{Ka} = \mathrm{K}(\delta_l^0/S_l^0)$ is the nondimensional stretch rate, or Karlovitz number, and $\mathrm{Ma} = \mathscr{L}/\delta_l^0$ is the Markstein number.

The flame stretch rate can be directly related to the kinematics of the flame surface. The flame displacement velocity is defined as the normal component of the relative velocity of the flame surface in respect to the flow. It differs from the laminar (planar) flame speed because of flame curvature and unsteadiness. Naming S_d the displacement speed and $\vec{u}_o$ the flow velocity of the unburned mixture in the vicinity of the flame surface, the local propagation velocity of the flame surface $\vec{v}_F$ is

$$\vec{v}_F = \vec{u}_o + S_d\vec{n}, \tag{4}$$

where $S_d\ \vec{n}$ is the displacement velocity and $\vec{n}$ is the normal unit vector at the flame surface, pointed to the unburned mixture side.

Figure 2 illustrates the effect of flame curvature on stretch rate. A uniform flow velocity field $\vec{u}_o$ is used for simplicity. Figure 2a presents a flame surface that is concave towards the unburned mixture. The tangent component of the flow velocity $\vec{u}_{o,t}$ points towards the vertex, thus resulting in flame compression. This effect is expressed by the tangential strain rate component. The tangent component of the flow velocity at the surface $\vec{u}_{o,t}$ decreases towards the vertex. Therefore, the tangential strain rate is negative, $\nabla_t \cdot \vec{u}_{o,t} < 0$, indicating flame compression. The normal strain rate depends on the normal component of the flow velocity and flame curvature. The normal component of the flow velocity at the surface $\vec{u}_{o,n}$ is negative and the curvature is also negative, $\kappa = \nabla \cdot \vec{n} < 0$. Then, the normal strain rate becomes positive, $(\vec{u}_o \cdot \vec{n})\ \kappa > 0$. For the convex surface, Fig. 2b, the tangential component of the flow velocity results in flame extension, which is confirmed by $\nabla_t \cdot \vec{u}_{o,t} > 0$. For the normal strain rate, the curvature is positive, $\kappa = \nabla \cdot \vec{n} > 0$, and $(\vec{u}_o \cdot \vec{n})\ \kappa < 0$.

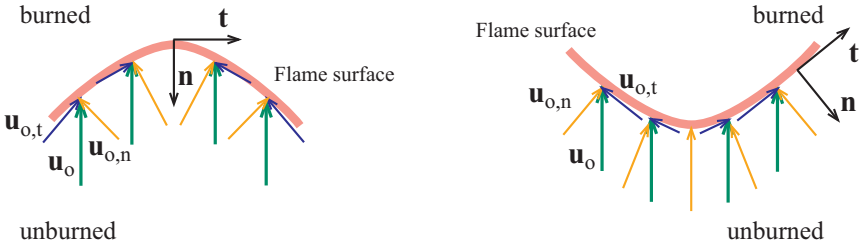

(a) Concave towards the unburned mixture:
$\kappa = \nabla \cdot \vec{n} < 0$
$\nabla_t \cdot \vec{u}_{o,t} < 0$
$(\vec{u}_o \cdot \vec{n})\ \kappa > 0$
$S_d(\nabla \cdot \vec{n}) < 0$

(b) Convex towards the unburned mixture:
$\kappa = \nabla \cdot \vec{n} > 0$
$\nabla_t \cdot \vec{u}_{o,t} > 0$
$(\vec{u}_o \cdot \vec{n})\ \kappa < 0$
$S_d(\nabla \cdot \vec{n}) > 0$

Figure 2: Effect of flame curvature on stretch rate. The green arrows are the flow field at the flame surface $\vec{u}_o$, assumed uniform, the yellow vectors are the normal component $\vec{u}_{o,n}$ and the blue vectors are the tangent component $\vec{u}_{o,t}$.

2.2 Hydrodynamic instability

The linear theory (for small disturbances) of flame instabilities was proposed, independly, in the works of Darrieus (1938) and Landau (1944). Their findings demonstrate that in the thin flame approximation, the planar deflagrations are unconditionally unstable. The Darrieus-Landau (DL) theory assumes that any perturbation, e.g. in the flame front area in Fig. 3 , $f = 0 + f^{'}$, can be modeled as,

$$f^{'} = A(x)\mathrm{e}^{(iky+\omega t)}, \tag{5}$$

which the amplitude of perturbation is A, k is the transverse wavenumber and ω is the growth rate.

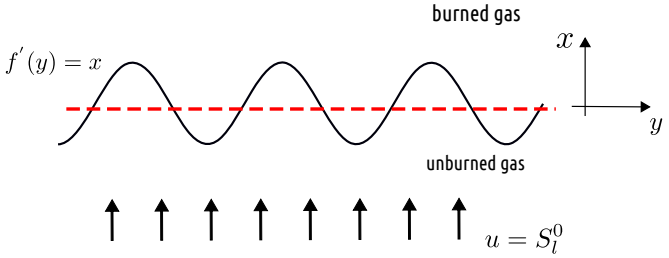

Figure 3: The perturbed surface of a planar flame.

The physical variables are also affected by the initial perturbation and can be written as $u = \overline{u} + u^{'}$, $v = \overline{v} + v^{'}$ and $p = \overline{p} + p^{'}$ where,

$$u^{'} = U(x)\mathrm{e}^{(iky+\omega t)}, \qquad v^{'} = V(x)\mathrm{e}^{(iky+\omega t)}, \qquad p^{'} = P(x)\mathrm{e}^{(iky+\omega t)}. \tag{6}$$

The capital letters identify the nominal values. The solution for ω yields,

$$\omega = \omega_{DL} S_l k, \qquad \omega_{DL} = \frac{1}{\sigma+1}(\sqrt{\sigma^3+\sigma^2-\sigma}-\sigma), \tag{7}$$

which $\omega_{DL}(\sigma)$ is a constant that depends on the density ratio between unburnt and burnt gases, $\sigma = \rho_u/\rho_b$. Since in combustion process, $\sigma > 1$, then $\omega_{DL} > 0$ and the initial disturbances will always grow in amplitude for all wavelengths. Moreover, the growth rate increases as k becomes larger, implying that the short waves grow faster than the long waves.

2.3 Thermo-Diffusive instability

As can be seen in experiments such as of Fig. 1, flames do not always evolve to wrinkled fronts. In order to take into account the thermo-diffusive effect to Darrieus-Landau theory, Eq. (7) was implemented by works performed by Pelce and Clavin (1988), Matalon and Matkowsky (1984) and Frankel and Sivashinsky (1982) yielding,

$$\omega = \omega_{\mathrm{DL}} S_l k - S_l \delta_l^0 [B_1 + \beta(\mathrm{Le}_{eff} - 1)B_2 + \mathrm{Pr}B_3]k^2. \tag{8}$$

Here, B_1, B_2 and B_3 are positive constants that depends solely on σ. These three terms correspond to thermal, molecular and viscous diffusion, respectively. The thermal and viscous coefficients tend to stabilize the perturbations. The molecular term can act towards destabilizing or stabilizing the front. It is controlled by the transport balance between species and heat diffusion represented by Lewis number depicted in Fig. 4. If the $\mathrm{Le} < 1$ and the flame front is convex towards the fresh gases, reactants diffuse towards burnt gases faster than heat diffuses toward the unburn gas. These reactants are heated and burn more quickly, increasing the local flame speed S_l, which is higher than flame speed S_l^0. On the other hand, for fronts convex towards the burnt gases, reactants diffuse in a large zone and the flame speed is decreased compared to S_l^0. This event increases the surface area. When the $\mathrm{Le} > 1$, the local flame speed tends to stabilize the front (decreasing the surface area). In the Eq. (8), the Lewis number is present as the effective Lewis number. This represents the average value of the fuel and oxidizer Lewis numbers weighted more heavily with respect to the deficient component in the mixture, (Matalon *et al.*, 2003).

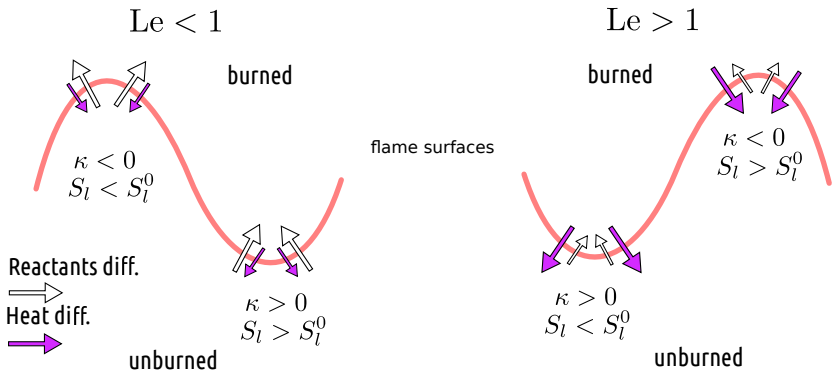

Figure 4: Effect of Lewis number and flame curvature, κ, on local flame speed, S_l.

3. MATERIALS AND METHODS

3.1 Computational Methods

In this work, direct numerical simulations are used to evaluate the role of hydrodynamic and thermo-diffusive instabilities in lean hydrogen/air premixed flames in order to measure their impact on local burning rate. The flow is modeled employing the finite volume method for Navier-Stokes equations at low-Mach limit. The computations were performed

using OpenFOAM's (OpenCFD, 2011) standard capabilities coupled to EBI-DNS (Engler-Bunte-Institute) implementation (Zirwes *et al.*, 2020) which address detailed transport coefficients to momentum, species and energy equations. The simulations employed the Li *et al.* (2004) reaction mechanism containing 9 species and 38 elementary reactions. In order to increase the time and spatial discretization accuracy, the backward difference method and cubic spatial interpolation schemes were used. Thereby, to keep the solution stable it was defined a $\mathrm{CFL} < 0.2$. The pressure-implicit split-operator (PISO) algorithm has been used for the pressure correction (Ferziger and Peric, 2002). The computational domains use rectangular structured meshes with at least 20 cells to resolve the flame thickness. Inlet conditions were prescribed while at the sides of the domain, periodic boundary conditions were imposed. To avoid reflections of pressure waves at the in- and outlet, non-reflective boundary conditions (NRBC) are used.

The study approaches two canonicals flames configurations, a Bunsen flame, and a planar flame, which are affected by different forms of stretch-chemistry interaction. Therefore, they are important sources of information to assess the role of each instability mechanism. Table 1 presents the laminar, planar, adiabatic flame parameters for the hydrogen/air flame solved with Cantera (Goodwin, 2002). In Tab. 1, $Y_{f,o}(\dot{q}'''_{max})$ is the value of the isoline of mass fraction for the definition of flame surface position. The τ_f is the the characteristic flame time defined as $\tau_f = \delta_l^0 / S_l^0$ and T_{ad} is the adiabatic flame temperature. For all simulations, the inlet boundary temperature is $T_u = 300$ K.

Table 1: Laminar, planar, adiabatic flame parameters for the hydrogen/air flames solved here ($T_u = 300$ K, $p = 100$ kPa).

ϕ	S_l^0, cm/s	δ_l^0, mm	τ_f, ms	T_{ad}, K	Le_{eff}	$Y_{f,o}(\dot{q}'''_{max})$
0.5	52.0	0.43	0.827	1646	0.51	0.00286
0.7	132.0	0.36	0.272	2021	0.69	0.00908

3.2 Configuration

Bunsen flames are highly stretched due to the effects of the flow field, making up regions dominated by strain and curvature deformation. These geometrical states are responsible for changing the transport gradients inside the flame structure, which evidences the flame deformation effects. The Bunsen flame was analyzed in steady-state condition with $\phi = 0.5$. The domain has a height of 20 mm in the stream-wise direction and 5 mm in width. A Poiseuille jet velocity profile is imposed in the inlet boundary with $\langle u \rangle = 3S_l^0$.

For planar flames, a set of simulations were carried out with the aim to study the behavior of linear and non-linear time evolution of initial perturbations imposed to initial planar flame. In all cases, the inlet velocity has a planar profile with $u = S_l^0$. For the linear analysis, the domain dimensions presents a constant length in streamwise direction of $l = 35\delta_l^0$, and different cases for crosswise direction were set up as $h = \lambda = 2\delta_l^0, 3\delta_l^0,\ 4\delta_l^0,\ 5\delta_l^0,\ 6\delta_l^0, 7\delta_l^0,\ 10\delta_l^0$ and $20\delta_l^0$ wich corresponds to normalized wavenumbers of $\hat{k} = 3.14, 2.094, 1.571, 1.256, 1.047, 0.898,\ 0.628$ and 0.314, respectively. A harmonic perturbation was introduced in temperature field, $T_p = T_0 \sin(ky)$ where $k = 2\pi/\lambda$. In this case, each domain has one wavelength and were studied flames with $\phi = 0.5$ and 0.7. To solve the non-linear problem, it was used a domain with 43 and 129 mm ($100\delta_l^0$ and $300\delta_l^0$) in streamwise and crosswise direction, respectively, yielding a mesh of $2150\ x\ 6450$ cells. Here, 60 wavelengths were initially imposed with $\lambda = 5\delta_l^0$ and $\phi = 0.5$.

4. RESULTS AND ANALYSIS

4.1 Highly stretched flames

Figure 5 presents the results for the Bunsen flame wherein Fig. 5a shows the normalized fuel reaction rate, and Figs. 5b and 5c depict the normalized flame consumption speed and Karlovitz number along the front, respectively. The flame consumption speed, S_c, is defined here by fuel consumption along the normal of the flame front,

$$S_c = \frac{1}{\rho_u (Y_{f,u} - Y_{f,b})} \int_{-\infty}^{+\infty} \dot{\omega}_f d\vec{n}. \tag{9}$$

where $Y_{f,i}$ is the fuel mass fraction in the unburned and burnt zones, and $\dot{\omega}_f$ is the fuel reaction rate. A visual inspection of Fig. 5a shows that the flame burns faster at the domain base reaching values of $4.5\tilde{\omega}_f$. Since hydrogen has the highest burning rate at the base, it provides an almost zero lift-off effect. Towards the top, the burning rate slows down until the flame extinction in the front.

The previous description is quantified in Fig. 5b. At the base, the flame S_c is almost 2.5 times than the flat flame speed. Up to $s/s_{max} = 0.3$, the S_c drops reaching a linear decay region between $0.3 > s/s_{max} > 0.8$. Near the tip, the S_c decreases exponentially. Graph 5c shows that the flame presents three distinct regions. In the first one, at the base, the

Ka is positive at the base where the front is positively curvate summed the flame-flow interaction that causes a tangential stretching. The second region is defined by a constant and weaker stretch rate. Near the tip, the negative curvature takes over the process resulting in a negative Ka.

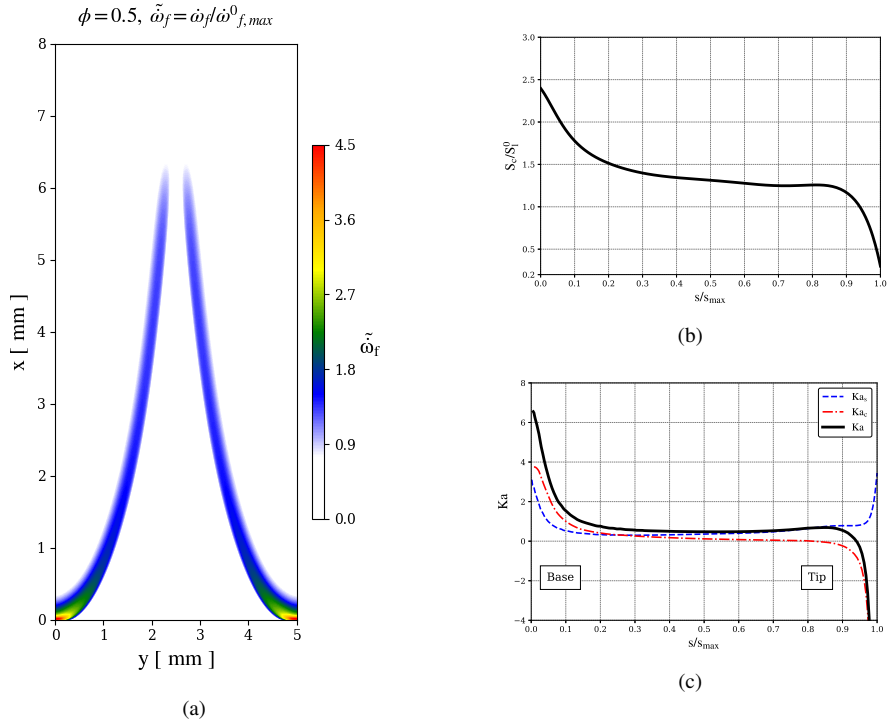

(a) (b) (c)

Figure 5: Simulation results for the Bunsen flame with $\phi = 0.5$, (a) normalized fuel reaction rate, (b) normalized consumption speed as a function of the nondimensional flame arc-length and (c) Karlovitz number as a function of the nondimensional flame arc-length.

Figure 6 shows the correlation of flame speed with the front deformation caused by the flow interaction. Figures 6a, 6b, and 6c depict the relation of flame speed, respectively, with the total Karlovitz number, the Ka due to the curvature, and related with the dimensionless curvature by the flame thickness. Unlike hydrocarbons, the hydrogen Ma is negative which means that the flame tends to increase the burning rate as the stretch rate also grows. Figures 6a and 6b reproduce the theoretical behavior. Near zero, flame behaves as is predicted for weak deformation theory where the flame speed varies linearly with the stretch as shown in the asymptotic correlation in Eq. (1). In the Figs. 6b and 6c is observed that a significant points quantity are located at $\mathrm{Ka_c} = 0$ ($\kappa = 0$), and out of this region, the flame speed is substantially affected by positive and negative stretch.

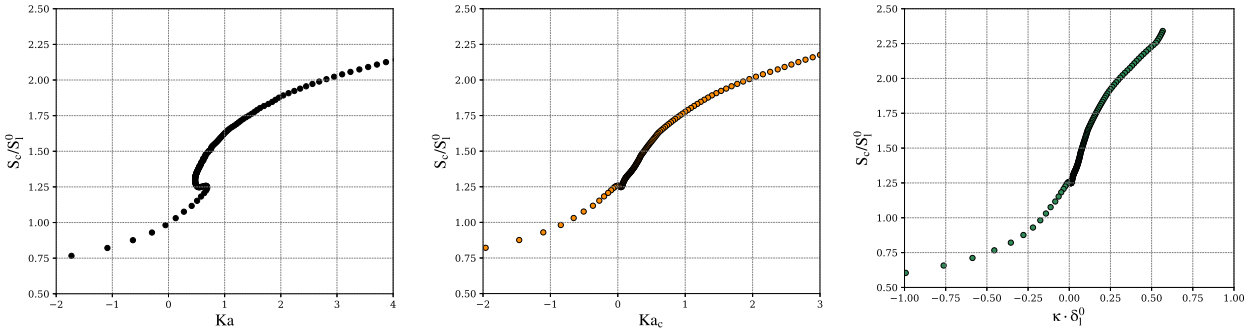

(a) (b) (c)

Figure 6: Bunsen flame correlation between flame consumption speed for $\phi = 0.5$ and, (a) Karlovitz number, (b) Karlovitz number due to curvature and (d) dimensionless curvature.

The flame quenching caused by the negative stretch can be explained by the effect of thermo-diffusive instabilities. The Le < 1 makes the thermo-diffusive mechanism unbalanced, where the fuel comes out from the front faster than

heat diffusion. The negatively curved flame surface leads to a defocused diffusion of hydrogen and a decreased local equivalence ratio. This effect cannot be compensated by the counteracting thermal diffusion, Zhang *et al.* (2017) and Poinsot and Veynante (2005). Figure 6a shows this effect in the deviation from the linear relation (1) for consumption speed far from unity. The reason for that is associate with the higher-order terms added by the curvature and Le < 1 interaction, Fig. 6c.

The stretch-diffusion relation is dominant in a Bunsen flame; however, the apparent hydrodynamic stability lies in its strong velocity tangential component in the flame surface. All structures on the flame surface are convected toward the flame tip at the tangential velocity, and thus have a finite residence time, $\tau = L/\vec{u}_{o,t}$, where L is the length of the slanted flame. This residence time must be compared with the growth time of instabilities $\tau = 1/\omega$. If the residence time is not large when compared with the growth time, then the small perturbations at the base will not have time to grow to an appreciable amplitude before they are convected out of the flame, Searby *et al.* (2009).

4.2 Planar flames

4.2.1 Linear growth

During the firsts propagation stages, the flame front perturbation grows linearly. The following results present the behavior of fuel isoline coming from DNS simulations. Figure 7 shows the amplification of initial perturbation for the case $\hat{k} = 0.628$ ($h = 10\delta_l^0$). In the beginning, in Fig. 7a, the perturbation profiles keep the sine form. Further, Fig. 7b, it can be observed that the diffusive effects take place and the profiles do not evolve homogeneously. For the convex region, $Y^{'} < 0$, the flame burns faster getting an extended low-curvature crest. On the other hand, in the concave region, $Y^{'} > 0$, the local flame speed is lower, which yields a trough-shaped flame structure with a depth increasing with temporal evolution.

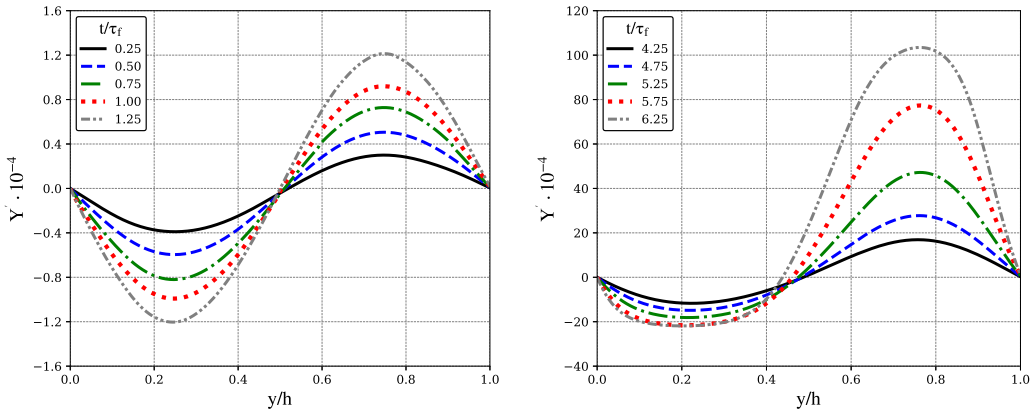

(a) (b)

Figure 7: Perturbation profiles for $\hat{k} = 0.628$ ($h = 10\delta_l^0$), (a) initial flame proagation, (b) thermo-diffusive effects.

Figure 8a reports the dimensionless dispersion relation, $\hat{\omega} = \omega \cdot \tau_f$, for the cases enumerated in section 3. Figure 8b complements the analysis illustrating the temporal evolution of the imposed initial amplification for three cases with $\phi = 0.5$. In the right graph is depicted the linear Darrieus-Landau coefficient and those computed by the simulations. The results are in line with those observed in the works of Altantzis *et al.* (2012) and Berger *et al.* (2019). The graph shows that for small wavenumbers, the growth rate tends to values predicted by hydrodynamic theory. However, the superimposed effect of diffusion ($\mathrm{Le_{eff}} < 1$) increases the $\hat{\omega}$. As the wavenumber gets larger, it reaches a maximum value, below ω_{DL}, and then, the growth rate becomes weaker towards negative values. In the last case, for $\hat{k} = 3.14$ ($h = 2\delta_l^0$) resulting in $\hat{\omega} = -1.78$, it is seen that for small wavelengths, the diffusion is able to damp the initial amplification rather than increase, seen in circle markers in Fig. 8b. Figure 8a also compares the growth rate of $\phi = 0.5$ and $\phi = 0.7$. The curves present the same qualitative characteristics described previously, although for all wavenumbers, $\phi = 0.5$ shows higher $\hat{\omega}$ even for the damping effect. According to the DL assumption, the amplification rate grows due to expansion factor and flame speed. However, the Le shows up having a substantial effect due to differential diffusion. The other models proposed by Pelce and Clavin (1988), Matalon and Matkowsky (1984) and Frankel and Sivashinsky (1982) added the diffusive effect which Altantzis *et al.* (2012) checked the accuracy of new approaches. They conclude that despite the models count with the second-order term, the growth rate is a physical process of higher-order.

In the results of the dispersion relation, a fourth order polynomial fit was used with the aim to map important features observed in the plot. For $\phi = 0.5$, the growth rate is null for $\hat{k} = 2.46$, $\hat{\omega}(2.46) = 0$. The hydrodynamic and the thermo-

diffusive instabilities have the same rate in $\hat{k} = 1.04$, $\hat{\omega}(1.04) = \hat{\omega}_{DL} = \hat{\omega}_{TD}$, and the growth rate has the a maximum value in $\hat{k} = 1.28$, $\hat{\omega}(1.28) = \hat{\omega}_{max}$. For $\phi = 0.7$, the $\hat{\omega}(2.52) = 0$, $\hat{\omega}(\hat{k} \to 0) = \hat{\omega}_{DL} = \hat{\omega}_{TD}$ and $\hat{\omega}(1.17) = \hat{\omega}_{max}$.

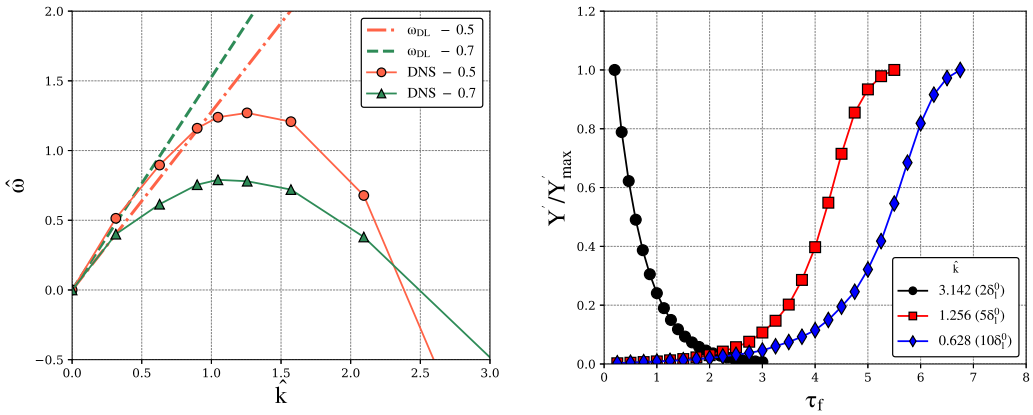

(a) (b)

Figure 8: Linear perturbations dynamic computed from the DNS simulations for $\phi = 0.5$, (a) dispersion relation comparison between hydrodynamic theory and simulations, (b) Time evolution of the initial perturbations for $\hat{k} = 1.257,\ 2.094$ and 3.14.

Figure 9 shows the instantaneous flame absolute speed, $Sa = \vec{v}_F \cdot \vec{n} = \vec{u} \cdot \vec{n} - S_d$, and the density-weighted flame displacement speed, taking two points of Fig. 7b, $t/\tau_f = 4.25$ (left column) and $t/\tau_f = 6.25$ (right column). In general, the absolute speed mirrors the displacement speed for both plots since the apparent front speed also decays as the displacement speed decreases, and the opposite is valid for regions where the burning rate increases. At $t/\tau_f = 4.25$, the harmonic profile remains. However, even with the low curvature, the local burning rate is affected. As time elapsed to $t/\tau_f = 6.25$, the scenario changes drastically. The fuel consumption response to negative curvature, Fig. 9d, makes the flow push the front backward while the positively curved remains propagation towards the inlet boundary. This dynamic is responsible for leading the flame front to chaotic behavior, causing the flame wrinkling analyzed in the following section.

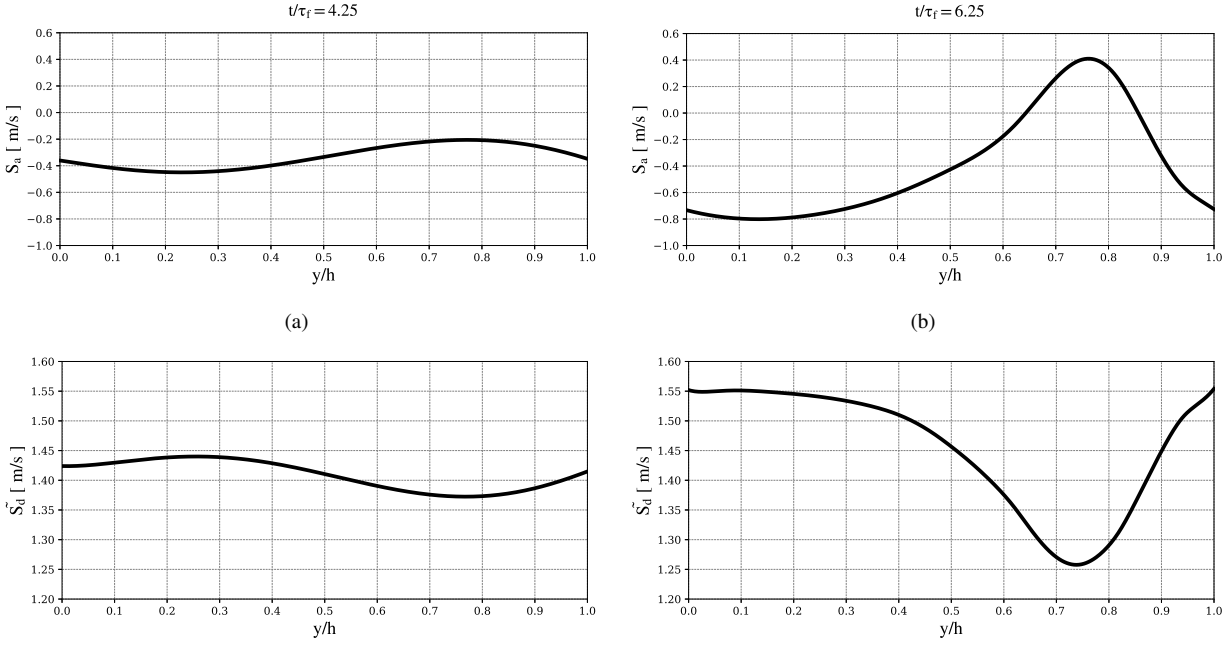

(a) (b)

(c) (d)

Figure 9: Flame speed profiles for the linear growth of initial perturbations with domain of $\hat{k} = 0.628$ ($h = 10\delta_l^0$), (a) absolute speed S_a at $t/\tau_f = 4.25$, (b) absolute speed S_a at $t/\tau_f = 6.25$, (c) displacement speed $\tilde{S}_d$ at $t/t_f = 4.25$ and (d) displacement speed $\tilde{S}_d$ at $t/\tau_f = 6.25$.

4.2.2 Non-linear growth

Figure 10 shows two time steps that present the flame front evolution in the broad domain for $\phi = 0.5$, during the linear growth, $t = 4.2\tau_f$, and the wrinking flame at $t = 26\tau_f$. Figures show the normalized temperature field $\tilde{T} = (T - T_u)/(T_a - T_u)$, and in Fig. 10d is seen, in a space magnification, the normalized heat release rate regarding the adiabatic flame, $\tilde{q} = \dot{q}'''/\dot{q}^{0}_{max}{}'''$. As was described in section 3.2, 60 wavelengths were imposed with $\lambda = 5\delta_l^0$, which were the fastest values found in the linear analysis.

At $t = 4.2\tau_f$, the harmonic waves keep the initial profile as reported in section 4.2.1. As the initial symmetry is broken, a wrinkled front is formed, composed of a broad range of small crests and trough-shapes geometries. In $t = 26\tau_f$, great wavelengths are present, made up of smaller ones that move forward and transversely, increasing the front area. It is observed in temperature field, regions with temperatures below the T_{ad}, and regions in superadiabatic conditions. Figure 10d shows a similar frame for the heat release rate. There are two highly curved regions, at right and left, that HRR has the order of $\tilde{q} = 0.5$, which decreases the flame propagation speed. On the other hand, it may be observed convex regions where the HRR can reach more than twice the value of the flat adiabatic flame.

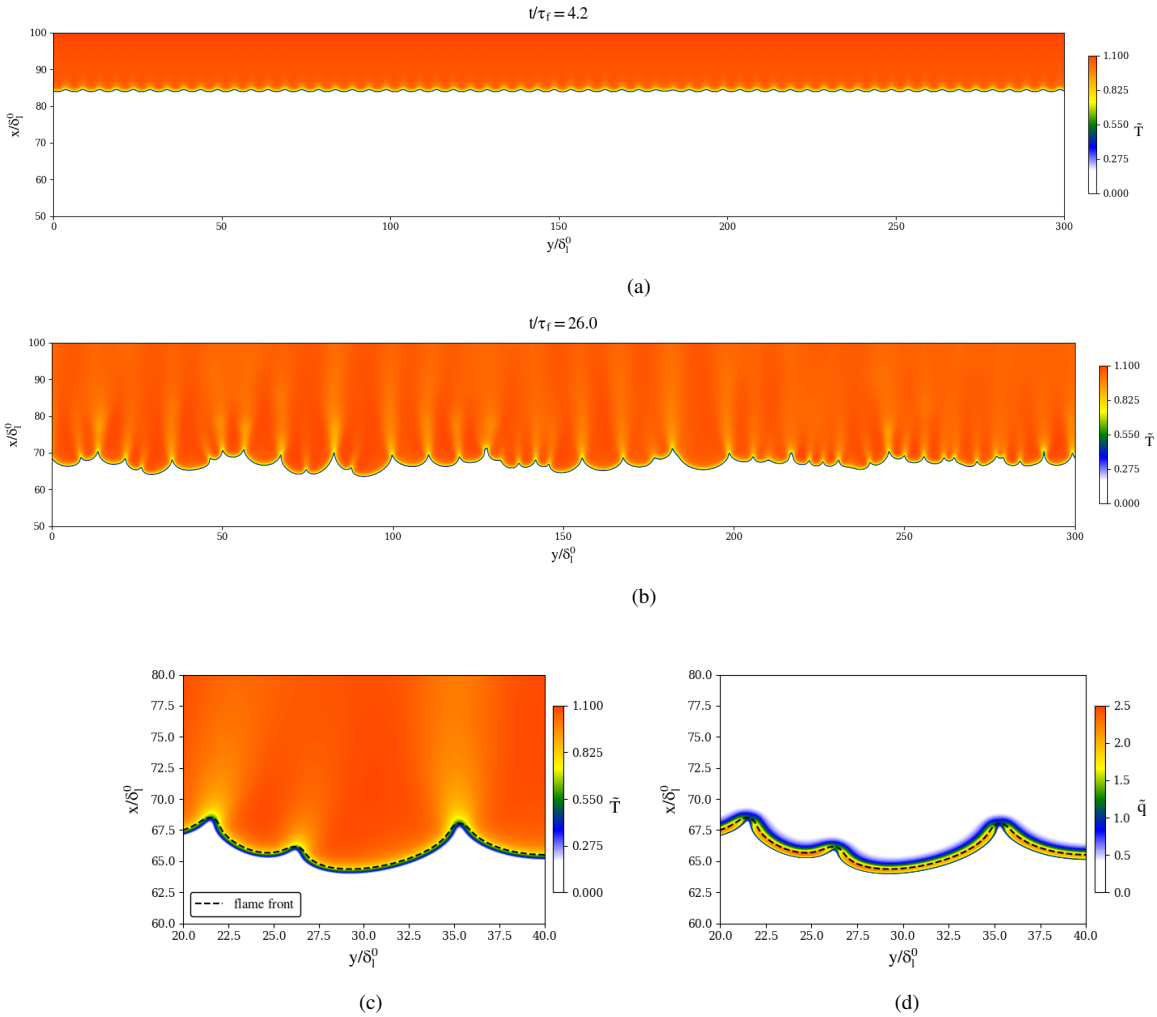

Figure 10: Time evolution of initial perturbations during the non-linear growth process, (a) temperature field at $t = 4.2\tau_f$, (b) temperature field at $t = 26\tau_f$, (c) temperature field magnified at $t = 26\tau_f$ and (d) heat release rate magnified at $t = 26\tau_f$.

Figure 11 presents the normalized curvature and burn properties highlighted in the black dashed line in Fig. 10c and 10d. In Fig. 11a is seen the flame curvature along the front arc-length, s, until $s/\delta_l^0 = 100$. It can be observed that the current front area surpasses the initial value of the flat flame since the geometry is highly curved, reaching 1.25 times the y-coordinate. Yet, it shows that there is a broad spectrum of curvatures at the front. It has ten deeper troughs resulting in stronger values of negative curvature. Positive curvature values are smoother and more extended as may be checked in graph 10b. Figure 11b shows the normalized consumption speed regarding the flat flame speed. The Figure depicts the effects of local curvature over the S_c. In regions where the negative κ is stronger, the normalized flame speed is much

lower than unity. On the other hand, for posivity κ, the S_c/S_l^0 may reach values of $1.6S_l^0$.

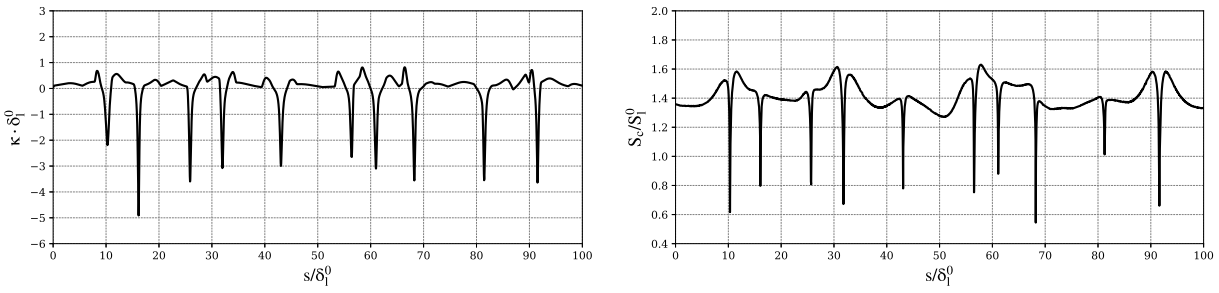

(a) (b)

Figure 11: Flame front structural properties, (a) flame curvature and (b) flame consumption speed.

The same correlation presented for the Bunsen flame curvature is shown for the current work frame in Fig. 12. The outcome forms a cloud of points with the higher concentration located above $\kappa = 0$, becoming less dense towards lower curvature values. The linear regression highlights that the Le effect over the Markstein number remains even with the chaotic flame behavior. Interestingly, exists a relation between Fig. 12 and Fig. 6c. Near $\kappa = 0$, the correlation for the Bunsen flame is linear (as predicted by Eq. (1)), and for the planar flame, the difference for linear behavior tends to decrease. For higher negative values, the deviation increases, and it is attributed to higher-order terms that the relation curvature-thermo-diffusive effects add to flame propagation dynamics.

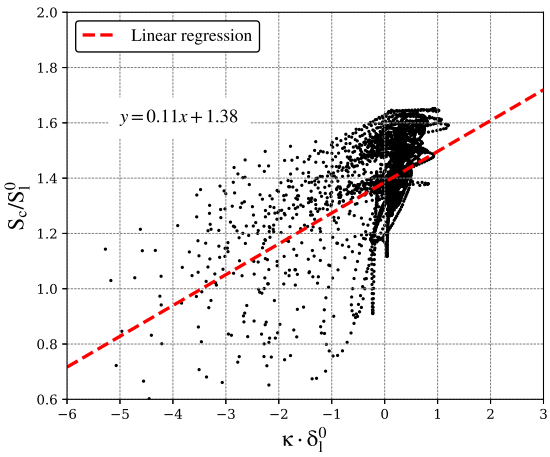

Figure 12: Correlation between dimensionless curvature and flame consumption speed for $\phi = 0.5$ at $t = 26\tau_f$ for the planar flame.

5. SUMMARY AND OUTLOOKS

Direct numerical simulations were carried out with lean hydrogen/air premixed flames to study the instability effect on two canonical flames, a Bunsen flame and planar flames in two-dimensional domains.

The Bunsen flame shows that stretch-chemistry and diffusion interaction substantially modify the local burning rate for sufficient lean mixtures. Positively curved regions may burn more than twice the flat flame speed, while negative curvature may cause the flame front extinction. At weaker stretched areas, the correlation of flame speed and Ka are in line with the linear theoretical model. However, far from these points, it was observed that the strain and curvature provide higher-order effects that cause significant deviation from linear theory.

For the planar flames, the outcomes show that the local flame speed depends on the growth rate, ω. The instabilities grow faster at a specific value of flame curvature related to the front wavelength. The dispersion relation presented for $\phi = 0.5$ shows that the $\lambda = 5\delta_l^0$ has the maximum growth rate value. For $\lambda = 2\delta_l^0$, the diffusive effects damp the initial perturbations. For a richer condition, $\phi = 0.7$, the lower Le tends to decrease the dimensionless $\hat{\omega}$. For the broad domain, the DNS simulation shows that the initial perturbations lead to a chaotic flame behavior where the wrinkled front is composed of a range of small crests and trough-shapes geometries, formed transversally by great wavelengths made

up of smaller ones. A linear regression, made with the correlation of curvature and consumption speed, showed that the deviation from the linear theory is lower for the smaller curved points, while for higher negative values, the deviation increases.

In the next steps of the work, the simulation for the broad domain will be performed until the curvature spectrum achieves statistical convergence. The characteristics of the front wavelengths can be surveyed, and then a flame wrinkling rate model can be built.

6. ACKNOWLEDGMENTS

The authors gratefully acknowledge the research group of Engler-Bunte-Institute, Division of Combustion Technology, Karlsruhe Institute of Technology, Germany, for providing the EBI-DNS solver. The support of the Scientific Computation Laboratory of Campus Joinville/UFSC, of the Graduate Program in Mechanical Engineering at Federal University of Santa Catarina, Brazil, the National Laboratory for Scientific Computing (LNCC/MCTI, Brazil) for providing HPC resources of the SDumont supercomputer, and the National Council for Scientific and Technological Development, Brazil, for the scholarship of the leading author.

7. REFERENCES

Altantzis, C., Frouzakis, C.E., Tomboulides, A.G., Matalon, M. and Boulouchos, K., 2012. "Hydrodynamic and thermodiffusive instability effects on the evolution of laminar planar lean premixed hydrogen flames". *Journal of Fluid Mechanics*, Vol. 700, p. 329–361.

Berger, L., Kleinheinz, K., Attili, A. and Pitsch, H., 2019. "Characteristic patterns of thermodiffusively unstable premixed lean hydrogen flames". *Proceedings of the Combustion Institute*, Vol. 37, No. 2, pp. 1879–1886.

Darrieus, G., 1938. "Propagation d'un front de flamme". *La Technique Moderne, unpublished*.

Ferziger, J.H. and Peric, M., 2002. *Computational Methods for Fluid Dynamics*. Springer, Berlin.

Frankel, M. and Sivashinsky, G., 1982. "The effect of viscosity on hydrodynamic stability of a plane flame front". *Combustion Science and Technology*, Vol. 29, pp. 207–224.

Goldmann, A., Sauter, W., Oettinger, M., Kluge, T., Schröder, U., Seume, J.R., Friedrichs, J. and Dinkelacker, F., 2018. "A study on electrofuels in aviation". *Energies*, Vol. 11, No. 2.

Goodwin, D.G., 2002. *Cantera C++ user's guide*. California Institute of Technology, California.

Jomaas, G., Law, C.K. and Bechtold, J.K., 2007. "On transition to cellularity in expanding spherical flames". *Journal of Fluid Mechanics*, Vol. 583, p. 1–26.

Kwon, O., Rozenchan, G. and Law, C., 2002. "Cellular instabilities and self-acceleration of outwardly propagating spherical flames". *Proceedings of the Combustion Institute*, Vol. 29, No. 2, pp. 1775–1783. ISSN 1540-7489.

Landau, L., 1944. "On the theory of slow combustion". In P. Pelcé, ed., *Dynamics of Curved Fronts*, Academic Press, San Diego, pp. 403–411. ISBN 978-0-12-550355-6.

Lhuillier, C., Brequigny, P., Contino, F. and Mounaïm-Rousselle, C., 2020. "Experimental study on ammonia/hydrogen/air combustion in spark ignition engine conditions". *Fuel*, Vol. 269, p. 117448. ISSN 0016-2361.

Li, J., Zhao, Z., Kazakov, A. and Dryer, F., 2004. "An updated comprehensive kinetic model of hydrogen combustion". *International Journal of Chemical Kinetics*, Vol. 36, pp. 566 – 575.

Masri, A., 2021. "Challenges for turbulent combustion". *Proceedings of the Combustion Institute*, Vol. 38, No. 1, pp. 121–155. ISSN 1540-7489.

Matalon, M., 2007. "Intrinsic flame instabilities in premixed and nonpremixed combustion". *Annual Review of Fluid Mechanics*, Vol. 39, pp. 163–191.

Matalon, M., Cui, C. and Bechtold, J., 2003. "Hydrodynamic theory of premixed flames: Effects of stoichiometry, variable transport coefficients and arbitrary reaction orders". *Journal of Fluid Mechanics*, Vol. 487, pp. 179 – 210.

Matalon, M. and Matkowsky, B., 1984. "On the stability of plane and curved flames." *SIAM Journal on Applied Mathematics*, Vol. 44, No. 2, pp. 327–343. ISSN 0036-1399.

Omari, A., Heuser, B., Pischinger, S. and Rüdinger, C., 2019. "Potential of long-chain oxymethylene ether and oxymethylene ether-diesel blends for ultra-low emission engines". *Applied Energy*, Vol. 239, pp. 1242–1249. ISSN 0306-2619.

OpenCFD, 2011. "Openfoam user guide". version 2.0.1.

Pelce, P. and Clavin, P., 1988. "Influence of hydrodynamics and diffusion upon the stability limits of laminar premixed flames". In P. Pelcé, ed., *Dynamics of Curved Fronts*, Academic Press, San Diego, pp. 425–443. ISBN 978-0-12-550355-6.

Poinsot, T. and Veynante, D., 2005. *Theorical and Numerical Combustion*. Edwards, Philadelphia, 2nd edition.

Searby, G., Candel, S., Durox, D., Schuller, T. and Dunn-Rankin, D., 2009. *Instability Phenomena during Flame Propagation*. ISBN 978-0-8493-8408-0.

Zhang, F., Zirwes, T., Habisreuther, P. and Bockhorn, H., 2017. "Effect of unsteady stretching on the flame local dynamics". *Combustion and Flame*, Vol. 175, pp. 170–179. ISSN 0010-2180. Special Issue in Honor of Norbert Peters.

Zirwes, T., Zhang, F., Habisreuther, P., Hansinger, M., Bockhorn, H., Pfitzner, M. and Trimisn, D., 2020. "Quasi-dns dataset of a piloted flame with inhomogeneous inlet conditions". *Flow, Turbulence and Combustion*, Vol. 104, pp. 997–1027.

8. RESPONSIBILITY NOTICE

The authors are solely responsible for the printed material included in this paper.